ADVANCED FUNCTIONAL MATERIALS
www.afm-journal.de

The Structural Origin of Chiroptical Properties in Perovskite Nanocrystals with Chiral Organic Ligands

Young-Hoon Kim, Ruyi Song, Ji Hao, Yaxin Zhai, Liang Yan, Taylor Moot, Axel F. Palmstrom, Roman Brunecky, Wei You, Joseph J. Berry, Jeffrey L. Blackburn, Matthew C. Beard, Volker Blum,* and Joseph M. Luther**

The authors investigate how chiral ligands attached to perovskite nanocrystal (PNC) surfaces structurally distort the perovskite lattice. Chiral electro-optical properties of the resulting PNCs are demonstrated through the fabrication of a circularly polarized light (CPL) detector with a discrimination of up to 14% between left- and right-handed CPL. Both experimental and electronic-structure-based simulations are combined to provide insights into the interactions (both structural and electronic) between chiral organic ligands and PNCs. The major finding is a centro-asymmetric distortion of the surface lattice that penetrates up to five atomic unit cells deep into the PNCs, which is the likely cause of the chiral-optical properties. Spin-polarized transport through chiral-PNCs results from the chiral-induced spin selectivity effect and amplifies the discrimination between left and right-handed CPL as is experimentally demonstrated in the detectors.

Y.-H. Kim, J. Hao, Y. Zhai, T. Moot, A. F. Palmstrom, R. Brunecky, J. J. Berry, J. L. Blackburn, M. C. Beard, J. M. Luther
National Renewable Energy Laboratory
Golden, CO 80401, USA
E-mail: matt.beard@nrel.gov; joey.luther@nrel.gov
Y.-H. Kim
Department of Energy Engineering
Hanyang University
Seoul 04763, Republic of Korea
R. Song
Department of Chemistry
Duke University
Durham, NC 27708, USA
L. Yan, W. You
Department of Chemistry
University of North Carolina at Chapel Hill
Chapel Hill, NC 27599, USA
V. Blum
Department of Chemistry
Thomas Lord Department of Mechanical Engineering and Material Science
Duke University
Durham, NC 27708, USA
E-mail: volker.blum@duke.edu
The ORCID identification number(s) for the author(s) of this article can be found under https://doi.org/10.1002/adfm.202200454.

DOI: 10.1002/adfm.202200454

1. Introduction

Colloidal metal halide perovskite nanocrystals (PNCs) provide an outstanding platform for exploring chirality-mediated electro-optical phenomena. This system combines the strong spin-orbit coupling (SOC) and controllable Rashba-Dresselhaus splitting in metal-halide perovskites[1–3] with the extensive tunability afforded by surface ligand attachment, which in this case can be chiral molecules. Systems such as colloidal $CsPbBr_3$ PNCs[4] have the potential to enable chiroptical and spin-selective phenomena in addition to the immense attention already devoted to optoelectronics, for example, photovoltaics[5] and light emitting diodes[6] in non-chiral counterparts. Chiral ligands attached to the surface of PNCs promote the controlled absorption and luminescence of circularly polarized light (CPL), which has been observed in colloidal solutions[7] and for PNCs dispersed in matrices such as polymethyl methacrylate.[8] Circular dichroism (CD) and circularly polarized luminescence can also be observed in PNCs helically arranged in chiral nano-helical media.[9,10] However, the physics behind the mechanism(s) by which chiral ligands or the surrounding media impart chiroptical response in PNCs is still ambiguous, which, in this work, we aim to understand more thoroughly.

Two mechanisms of chiral transfer in colloidal PNCs have been discussed. Waldeck and coworkers suggested that chiral surface ligands transfer chirality to the PNCs mostly through electronic coupling, either by: 1) the formation of a charge transfer state between the chiral ligands and the PNCs; or 2) imprinting chirality onto PNC's excitonic states.[11] Both mechanisms are specifically electronic interactions. Duan and coworkers report that chiral amine ligands bind with surface Br-rich defects and structurally transfer the chirality into PNCs by inducing asymmetric lattice distortions on the perovskite surfaces.[8] These studies provide conceptual ideas for possible chirality transfer mechanisms in PNCs. However, a more fundamental understanding is needed of both the possible electronic and structural interactions between the chiral ligands and metal-halide PNCs. The electronic properties of Pb-halide based perovskites are largely determined by the inorganic Pb-halide interconnected $[PbX_6]^{4-}$ octahedra.[12] Surface ligands can affect the electronic properties of PNCs through both

structural distortions of the underlying PNCs and electronic interactions between the organic and inorganic components, and it is generally difficult to isolate electronic versus structural interactions.

To gain better understanding of the origins and magnitude of chiroptical activity in PNCs with chiral ligands, here we combine an experimental photophysical investigation with high fidelity computational simulations of the interaction between chiral organic ligands and PNCs. We employed density function theory (DFT) to study the structural distortion within perovskite slab models with chiral ligands terminating the surfaces. The simulations show that surface-attached R-/S-methylbenzylammonium bromide (R-/S-MBA:Br) induces a centro-asymmetric distortion in the five outermost Pb-Br octahedra in colloidal Cs-lead bromide ($CsPbBr_3$) nanocrystals. We propose that such distortion imparts chirality into PNCs and induces chiroptical activity (CD) from the PNCs. We pair these chiral-functionalized PNC films with semiconducting single-walled carbon nanotubes (SWCNTs) to demonstrate a heterojunction-based CPL detector which has CPL selectivity of up to 14%.

2. Results and Discussion

Figure 1a,b show cartoons depicting cubic colloidal PNCs without (Figure 1a) and with (Figure 1b) chiral MBA ligands on the nanocrystal surfaces. DFT simulations suggest the outermost layers of lead bromide octahedra are distorted by the chiral ligands, as depicted in Figure 1b and discussed in more detail below.

To confirm the ligands are attached on the PNC surfaces, we study the surface chemistry of S-MBA:Br-treated $CsPbBr_3$ PNCs (hereafter referred to as S-PNCs) by conducting ^1H NMR (Figure S1, Supporting Information). Here, we used ferrocene as a control molecule to calculate the S-MBA:Br density on the S-PNC surfaces. First, pristine $CsPbBr_3$ PNCs (without chiral ligands) show peaks at chemical shifts (δ) of ≈0.8, 1.18, 1.45–1.55, 1.95, 2.3, 3.2, and 5.3 ppm, which are in accordance with previous literature[13–15] and indicative of the native oleate and oleylammonium ligands present on the PNC surfaces. The S-MBA:Br ligands exhibit distinct and sharp peaks at $\delta \approx 1.65$, 4.38, and 7.2–7.5 ppm. In S-PNC samples, peaks which were originally positioned at $\delta \approx 7.2$–7.5 ppm in S-MBA:Br samples are broadened and shifted downfield, indicative of the chemical interaction between S-MBA:Br and PNC surfaces (Figure S1b, Supporting Information). We conclude that a ligand density of about 1.96 ligand nm^{-2} of S-MBA ligands is attached to the S-PNC surface upon ligand treatments (see the Supporting Information for further discussion). Fourier transform infrared (FTIR) data further confirm the existence of chiral molecules on the PNCs after ligand treatments (Figure S2, Supporting Information).[16]

Because surface ligands, in general, can significantly affect the excitonic recombination dynamics in PNCs, we measured photoluminescence (PL) quantum efficiency (QE) of control PNC and R-/S-PNC films. The R-/S-MBA:Br treatment of the $CsPbBr_3$ PNC films increases the PLQE from 10.9% for control samples to values around 24% (**Figure 2**a). The inset of Figure 2a shows photographs displaying brighter emission of R-/S-PNC films than that of control PNC films under UV light excitation. We also found that rac-MBA:Br treatment (here, rac- means mixture of R- and S- ligands with equal molar ratio) improves the PLQE up to 14.7%. A PLQE increase generally happens via passivation of surface defects as depicted in Figure 1b and this lends further proof to the ligands interacting with the surface.

To investigate the recombination dynamics of charge carriers in the $CsPbBr_3$ PNC films upon R-/S-MBA:Br ligand treatment, we measured PL lifetime of samples using time-resolved PL (Figure 2b). We fit the PL transients using a biexponential decay (sum of short-lived and long-lived components that give a short lifetime (τ_1) with intensity (A_1) and a long lifetime (τ_2) with intensity (A_2), respectively) and calculate the average PL lifetime by intensity weights ($\tau_{ave} = (A_1 \times \tau_1 + A_2 \times \tau_2)/(A_1 + A_2)$) (Figure S3, Table S1, Supporting Information). Control PNCs showed faster decay at <2 ns compared to R-/S-PNCs

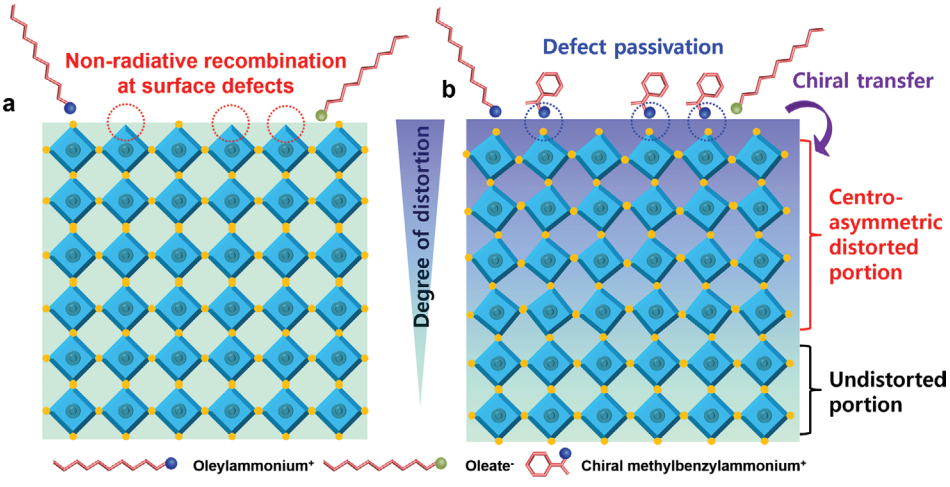

Figure 1. Schematic illustrations of a) colloidal PNCs without chiral ligands and b) chiral transfer mechanism in surface-functionalized colloidal PNCs with chiral ligands. Schematics illustrate that chiral surface ligands transfer chirality into PNCs by inducing centro-asymmetric distortion on the PNC surfaces and passivate the surface defects.

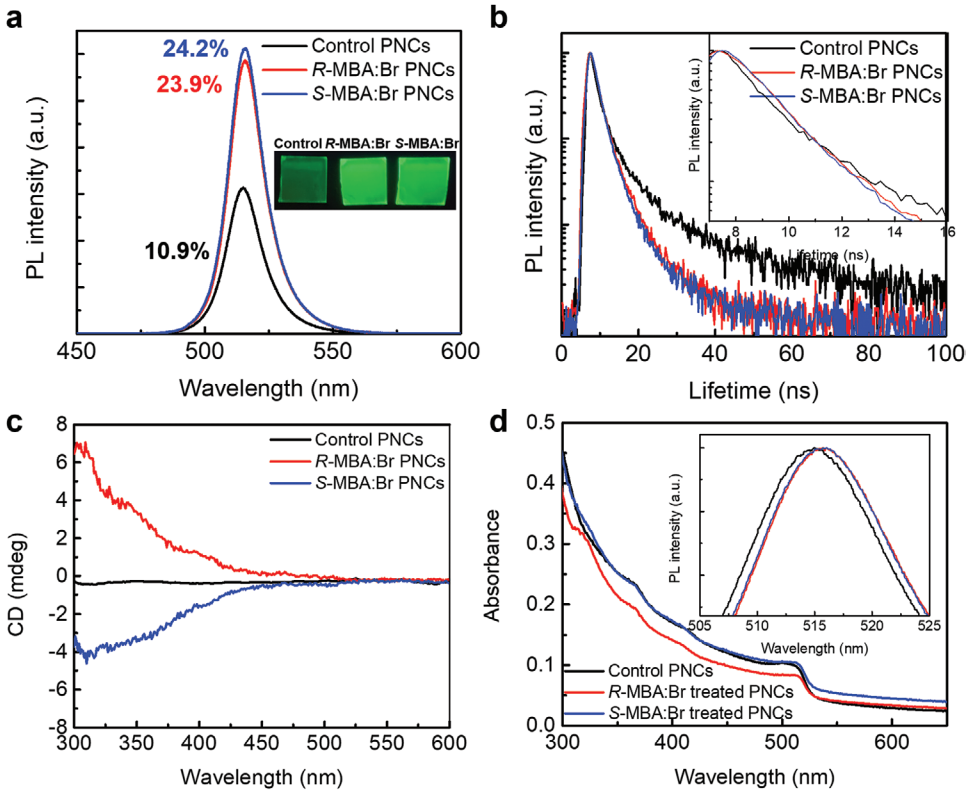

Figure 2. a) PL spectra, PLQE values, and luminescence images (inset) and b) PL lifetime decays of native-ligand capped (control, without chiral ligands) PNC films and R-/S-MBA:Br-treated PNC films (inset of (b) shows magnified PL lifetime decays). Here, black, red, and blue lines are data from control PNCs, R-MBA:Br-treated PNC films, and S-MBA:Br-treated PNC films, respectively. c) Circular dichroism (CD) spectra and d) absolute absorbance of native-ligand capped (control) PNC films and R-/S-MBA:Br-treated PNC films. Inset of panel (d) shows magnified PL spectra of native-ligand capped (control) PNC films and R-/S-MBA:Br-treated PNC films.

due to ultrafast quenching or initial trapping of charge carriers in defects (inset of Figure 2b).[17,18] Interestingly, control PNCs showed drastically increased long-lived components (τ_2 = 10.88 ns, A_2 = 1.69) compared to R-/S-PNCs (τ_2 = 6.48 ns, A_2 = 0.2 for R-PNCs, τ_2 = 7.45 ns, A_2 = 0.12 for S-PNCs); we attribute this change in the long-lived components as delayed radiative recombination of charge carriers in control PNCs due to multiple trapping and detrapping of charge carriers in the unpassivated defect states.[17]

With fitted average PL lifetimes, we calculate the radiative recombination rate K_r and non-radiative recombination rates K_{nr} of each PNC film by considering average PL lifetime and PLQE with the below equations,

$$\frac{1}{K} = \frac{1}{K_{nr} + K_r} \quad (1)$$

$$PLQE = \frac{K_r}{K_{nr} + K_r} \quad (2)$$

where K is a PL decay rate (reciprocal of PL lifetime). Control PNC films show $K_r \approx 0.0826$ ns^{-1} and $K_{nr} \approx 0.677$ ns^{-1}. R-/S-PNC films show increased K_r and reduced K_{nr} ($K_r \approx 0.167$ ns^{-1} and $K_{nr} \approx 0.532$ ns^{-1} for R-PNCs, $K_r \approx 0.163$ ns^{-1} and $K_{nr} \approx 0.512$ ns^{-1} for S-PNCs) (Table S2, Supporting Information). These results indicate that R-/S-MBA:Br chiral ligands facilitate the radiative recombination of charge carriers while suppressing non-radiative recombination of charge carriers by passivating surface defects, unlike 2D bulk perovskites, in which chiral A-site cations completely extinguish PL at room temperature.[19]

R-/S-PNC films show CD features below 515 nm (optical bandgap of the PNCs) with opposite signs according to the chirality of ligands (Figure 2c). Although the CD signals between 450 and 515 nm in R-/S-PNC films are relatively small, possibly due to weak absorption at 515 nm (weak contribution from exciton transition) (Figure 2d),[20] the fact that pure R-/S-MBA:Br ligands dispersed in ethyl acetate (EtOAc) show CD onsets at 275 nm (Figure S4, Supporting Information) and control samples of PNC films without R-/S-MBA:Br ligands and rac-PNC films do not show noticeable CD features (Figure 2c, Figure S5, Supporting Information) indicates that R-/S-MBA:Br ligands induce a chiroptical response in $CsPbBr_3$ PNCs and the CD signals track the nanocrystal absorption between 275 and 515 nm (the regime beyond absorption of untethered R-/S-MBA:Br ligands).

Next, we investigate the major contributing mechanism by which chiral ligands impart chiroptical response in PNCs. To distinguish between electronic interactions[11] and structural transfer[8] which were previously reported as chiral transfer mechanisms in colloidal PNCs (Table S3, Supporting Information), we study in detail changes in the optical bandgap and lattice parameter upon addition of the

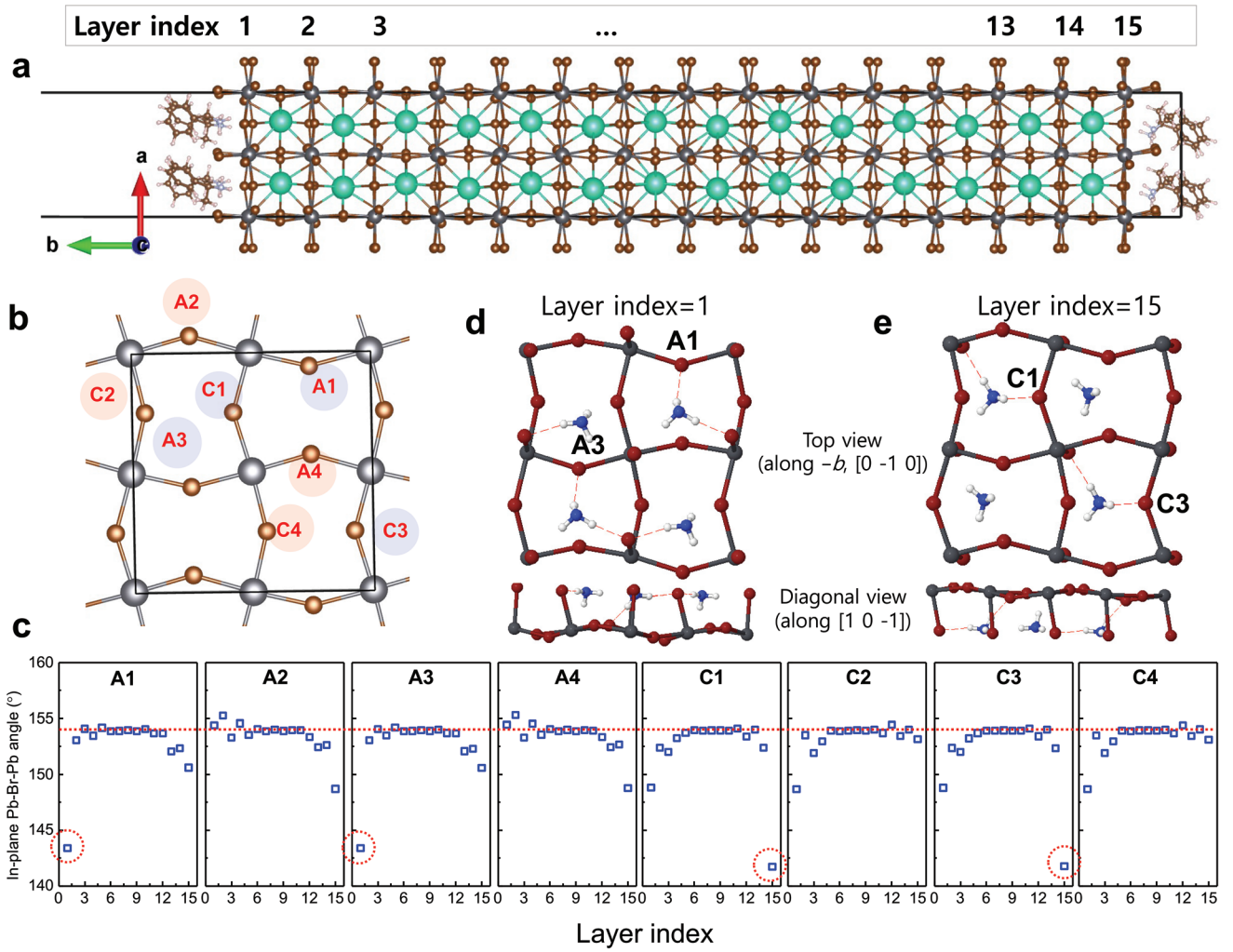

Figure 3. a) DFT-derived 15-layer inorganic slab models of perovskite crystals with $[S\text{-}MBA]^+$ ligands attached on opposite crystal surfaces. b) (010) plane of the simulated bulk $CsPbBr_3$ perovskite (orthorhombic) crystal structures labeling various calculated Pb-Br-Pb bond angles. c,d) show the centro-asymmetric hydrogen-bond-like interactions between MBA ligands (ammonium group) and Br^- in c) layer index = 1 and d) layer index = 15. Here, the top images are top-views along the (–*b*) direction and bottom images are diagonal views along the [1 0 $\bar{1}$] direction. e) Calculated layer-dependent bond angles of perovskite crystals with S-MBA ligands attached on the opposing surfaces. Here, red dashed circles highlight the centro-asymmetric crystal distortion induced by S-MBA ligands.

chiral-ligands. Typically, passivation of sub-gap defect levels by a ligand treatment should induce a blueshift of absorption and PL spectra.[21] Furthermore, an increase of the particle size and/or aggregation/agglomeration of particles would generally increase the PL lifetime and decrease the PLQE because spatial confinement of charge carriers in colloidal particles is reduced.[22] On the contrary, the R-/S-MBA:Br ligands induce a slight redshift of both the absorption and PL spectra (i.e., indicating a decrease of the optical bandgap) while simultaneously increasing PLQE and decreasing PL lifetime (Figure 2a,b,d and discussion). R-/S-MBA:Br ligands reduce the lattice parameter from 5.86 to 5.84 Å as calculated by considering shifts of all X-ray diffraction maximum peak positions, while maintaining the original crystal structure (Figure S6, Supporting Information and associated discussion). This observation implies that the chiral ligands shrink the inorganic octahedral lattice; a structural distortion can explain both the decreased optical bandgap and induced chirality in $CsPbBr_3$ PNCs (Figure 2c).

To visualize and model the effects of R-/S-MBA:Br ligands on the crystal structure of $CsPbBr_3$ PNCs and elucidate the observed bandgap narrowing inside the PNCs, we performed DFT calculations based on the semilocal PBE[23] functional with the Tkatchenko–Scheffler (TS)[24] van der Waals (vdW) correction and modified vdW radii for Cs (see Experimental Section and Tables S4,S5, Figures S7,S8, Supporting Information for details; we refer to the overall method as "PBE + TS-Cs" for short). We construct 15-layer $CsPbBr_3$ slabs with (2 × 2) unit cell with respect to the lattice defined by Pb sites, with surfaces parallel to (010) lattice planes (**Figure 3**a) of the fully computationally relaxed (DFT-PBE + TS-Cs) orthorhombic $CsPbBr_3$ bulk structure (Table S5, Supporting Information). To simulate $CsPbBr_3$ nanocrystal surfaces with chiral ligands, $[S\text{-}MBA]^+$ cations are placed on opposite slab surfaces, replacing the

corresponding Cs^+ cations (A-site substitution). A 15-layer simulation corresponds approximately to 10 nm slab of a nanocrystal to coincide with the samples used in experimental analysis (Figure S9, Supporting Information). While we do not know the specific molecular adsorption geometry at the surface a priori, a recent, detailed crystallographic study of hydrogen bonding and structural chirality transfer in layered 1-(1-naphthyl)ethylammonium (NEA) lead bromide[25] suggests a possible adsorption pattern with a propensity for transferring ligand-chirality to the lead bromide octahedral planes and is used as a basis for setting up the present models. The resulting input geometries feature a charge neutral unit cell and a centrosymmetric ligand adsorption. We computationally optimized the geometry to reflect a local minimum of the Born–Oppenheimer potential energy surface, with gradients below 5×10^{-3} eV Å^{-1} in magnitude. After optimization, interoctahedral Pb-Br-Pb bond angles as labeled in Figure 3b are employed as a measure of the overall surface distortion compared to the orthorhombic bulk structure. There are 8 Pb-Br-Pb bond angles and total of 16 Pb-Br nearest-neighbor in-plane bonds (4 Pb-Br octahedra with 4 in-plane bonds each) in each layer parallel to the surface.

In Figure 3e, we show the resulting in-plane Pb-Br-Pb angles in different layers, that is, as a function of depth. The computationally relaxed $CsPbBr_3$ slabs with $[S\text{-}MBA]^+$ ligands show a large difference of the bond angles in the outermost layer, compared to the bulk value of 154.0° (Figure 3e). Moving toward deeper layers, the in-plane bond angles between adjacent octahedra gradually converge to ≈154° at approximately the 5th layer and below. Correspondingly there are noticeable bond angle distortions from 15th layer (i.e., the opposite slab surface) to 10th layer. The bond angle distortions induced by the absorbed $[S\text{-}MBA]^+$ cations are 90° rotated between opposite surfaces in this model: significant distortions occur at the A1 and A3 Pb-Br-Pb angles on the top surface (layer index 1), with counterparts at the C1 and C3 bond angles on the bottom surface (layer index 15), which form a global centro-asymmetric pattern (Figure 3c,d). This symmetry difference agrees with previously reported S-NEA lead bromide incorporated 2D perovskite bulk crystals, which also showed that R-NEA induced an equivalent symmetry difference with opposite direction in perovskite crystals.[25] In contrast, an inorganic slab model without $[S\text{-}MBA]^+$ ligands (i.e., with Cs^+ ions at the surface) leads to much more evenly distributed bond angle distortions and a globally centrosymmetric pattern (Figure S10, Supporting Information). As a further comparison, we also show that a racemic arrangement $[rac\text{-}MBA]^+$ (modeled after the known bulk structure of racemic NEA lead bromide)[25] of MBA cations on the surfaces induces much smaller and less penetrating distortions (for instance, 1.78° distortion in A1 bond angle for rac-MBA versus 10.33° distortion in A1 bond angle for S-MBA, 3 layers into slab for rac-MBA versus 5 layers for S-MBA) and forms a centrosymmetric bond angle pattern (Figure S11, Supporting Information), unlike S-MBA, which forms a centro-asymmetric pattern (Figure 3e). These results indicate that surface-adsorbed chiral ligands can induce a centro-asymmetric distortion in $CsPbBr_3$ nanocrystals that persists to the 5th layer and ultimately induces a structural chirality in PNCs, indicating support for the structural chiral transfer mechanism in PNCs.[8]

We next explore the energy band structure of the $CsPbBr_3$ 15-layer slab models with and without $[S\text{-}MBA]^+$ ligands on their surfaces calculated using the Heyd–Scuseria–Ernzerhof (HSE06) hybrid density-functional[26] (with 25% Hartree–Fock exchange and a screening parameter of 0.11 bohr^{-1}) and second-variation non-self-consistent SOC.[27] Large vacuum intervals (80 Å) separate the adjacent slabs along their stacking direction (*b* axis, **Figure 4**a) and thus a meaningful periodicity of a single slab exists along the *a* and *c* axes. Subsequently, we sampled the featured high symmetry points and k paths in the (a^*–c^*) plane of the Brillouin zone (Figure 4b) for band plotting, which corresponds to the (*a*–*c*) plane in real space. Band structures (Figure 4d–f) indicate that the band edges consist of the inorganic components (Br for valance band maximum and Pb for conduction band minimum at the Γ point). We also decomposed the electronic bands at the Γ point into contributions from the Pb atoms of each layer (Figure 4c,f), using a Mulliken decomposition. Interestingly, the plotted layer-dependent contribution of the states near the band edge (Figure 4c) resembles a textbook quantum well. For the lowest conduction band, the largest contributions are from the inner layers away from the distorted surfaces.

We also observe a ≈10 meV bandgap narrowing induced by the $[S\text{-}MBA]^+$ ligands relative to Cs^+ terminated slabs similar to the experimentally observed redshifts of the optical bandgap (Figure 2d). We note that the simulations compare Cs^+ to $[S\text{-}MBA]^+$ whereas the experiments compare native oleate and oleylammonium ligands termination to $[S\text{-}MBA]^+$ termination.

The computationally determined, centro-asymmetrically distorted Pb-Br planes provide clear evidence that a transfer of chirality between adsorbate molecules and PNCs can occur by way of a structural interaction between the $[PbBr_6]^{4-}$ connected octahedra and the chiral ligands. We also considered the electronic coupling between R-/S-MBA:Br surface ligands and PNCs such as the formation of a charge transfer band[11] (for which we have no evidence, see below) that can contribute to the chiral response of the PNCs, but conclude that the structural distortions are likely the largest contribution. The bandgap of R-/S-MBA:Br (≈4.5 eV, determined by considering the optical onset of 275 nm and excluding excitonic effects) is much larger than that of $CsPbBr_3$ PNCs (≈2.4 eV, determined by considering the optical onset of 515 nm), which reduces the possibility of electronic interaction between ligands and PNCs especially at the band edges of PNCs (≈515 nm).[28] Furthermore, our computational simulations indicate that the organic content in the frontier bands (mainly contributed by Pb and Br) is not detectable (<0.1%). As a result, we can conclude that a charge transfer band does not exist in our R-/S-PNCs at the band edges[11] although it could contribute to the response at higher energies.

To demonstrate the utility of surface-functionalized PNC films with chiral ligands, we fabricated in-plane two-terminal CPL detectors based on heterojunctions formed between R-/S-/control $CsPbBr_3$ PNCs (50 nm) and highly enriched (6,5) semiconducting SWCNT thin (10 nm) films (**Figure 5**a). The schematics of the measurement setup and heterojunction-based CPL detectors are described in Figure S12, Supporting Information and Experimental Section. First, we measured the transfer characteristics of the field-effect transistors (FETs) (V_{DS} = 3 V, V_{GS} = −30 to 30 V) using a non-polarized laser.

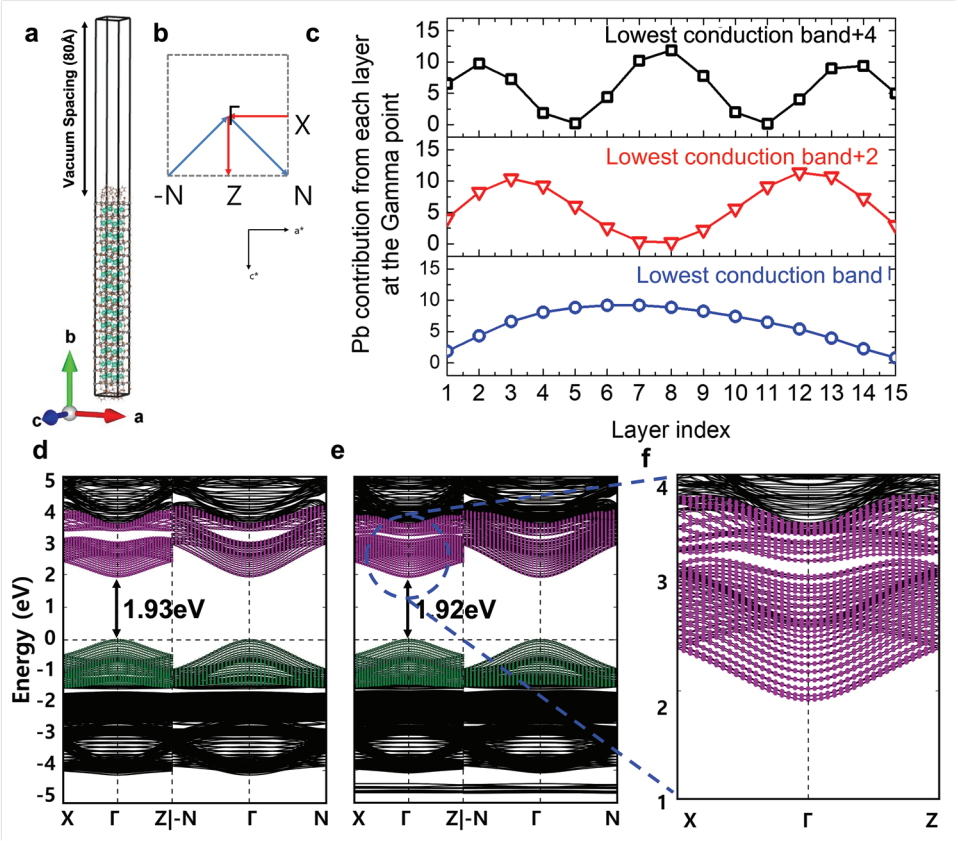

Figure 4. a) 3D view of the entire supercell of the $CsPbBr_3$ 15-layer slab model with $[S\text{-}MBA]^+$ ligands attached on opposite surfaces. b) High-symmetry points and *k*-space paths included in the band structures of $CsPbBr_3$ 15-layer slab models. c) Pb contribution in each band (lowest conduction band, lowest conduction band + 2, lowest conduction band + 4) at the Gamma point. Simulated energy bands of $CsPbBr_3$ 15-layer slab models d) without S-MBA ligands and e) with S-MBA ligands. Simulation results show a decrease of the bandgap (≈10 meV) upon adsorption of S-MBA ligands on the $CsPbBr_3$ crystals. f) Band structure near the lowest conduction band of $CsPbBr_3$ 15-layer slab models with S-MBA ligands.

Upon laser illumination, the threshold voltage shifts to positive voltage compared to that in the dark environment; this result indicates that photo-excited hole carriers generated from PNCs are transferred to SWCNT films due to electrical conductivity and hole carrier mobility in SWCNT layer, which results in p-type doping in SWCNT (Figure S13, Supporting Information).

Here, the chiral $CsPbBr_3$ PNC layers absorb circularly polarized photons and interfacial hole transfer to the highly conductive SWCNT layer promotes the transduction of CPL into electrical current.[29,30] After interfacial charge separation, ions in PNCs migrate to SWCNT layers with recovery of migrated ions (i.e., back diffusion) displaying very long time constants (>30 min) and this persistent photoconductivity results in current steps for each laser excitation.[29] Photo-transistors based on R-PNC/SWCNT heterostructures showed higher photocurrent change ($I_{ph} = I_{light} - I_{dark}$ where I_{light} is the source–drain current under light illumination and I_{dark} is the dark current) when excited by right-handed CPL while photo-transistors based on S-PNC/SWCNT heterostructures showed higher I_{ph} when excited by left-handed CPL (Figure 5b–d). These anisotropic photocurrent responses in photo-transistor devices are due in part to the controlled absorption of CPL in R-/S-PNC films (spin-selection mechanism (1) in Figure 5a). Based on the I_{ph} values measured under right- and left-handed CPL, we calculated the anisotropy *g*-factor of photocurrent (g_{ph}) from the following equation:

$$g_{ph} = 2 \times \frac{I_{ph,R} - I_{ph,L}}{I_{ph,R} + I_{ph,L}} \quad (3)$$

where $I_{ph,R}$ and $I_{ph,L}$ are the photocurrent responses under right-handed and left-handed CPL illumination, respectively. For checking the reliability of our devices, we compared the signals of devices under right-handed and left-handed CPL illumination at each measurement time and calculated the average g_{ph} with standard deviations. Photo-transistors based on R-PNC/SWCNT heterojunctions and S-PNC/SWCNT heterojunctions exhibit an average g_{ph} of 0.143 ± 0.028 and –0.089 ± 0.020, respectively (Table S6, Supporting Information). The higher absolute value of g_{ph} in R-PNCs/SWCNT heterojunctions, although consistent with higher CD spectrum in R-PNC films (Figure 2c), is within the error bars shown in Figure 5b. Photo-transistors based on non-chiral control PNC/SWCNT heterojunctions showed negligible anisotropy in the photocurrent responses to right-handed CPL and left-handed CPL illumination (Figure S14, Supporting Information).

It is worth noting that the g_{ph} of photo-transistors based on R-PNC/SWCNT heterojunctions and S-PNC/SWCNT

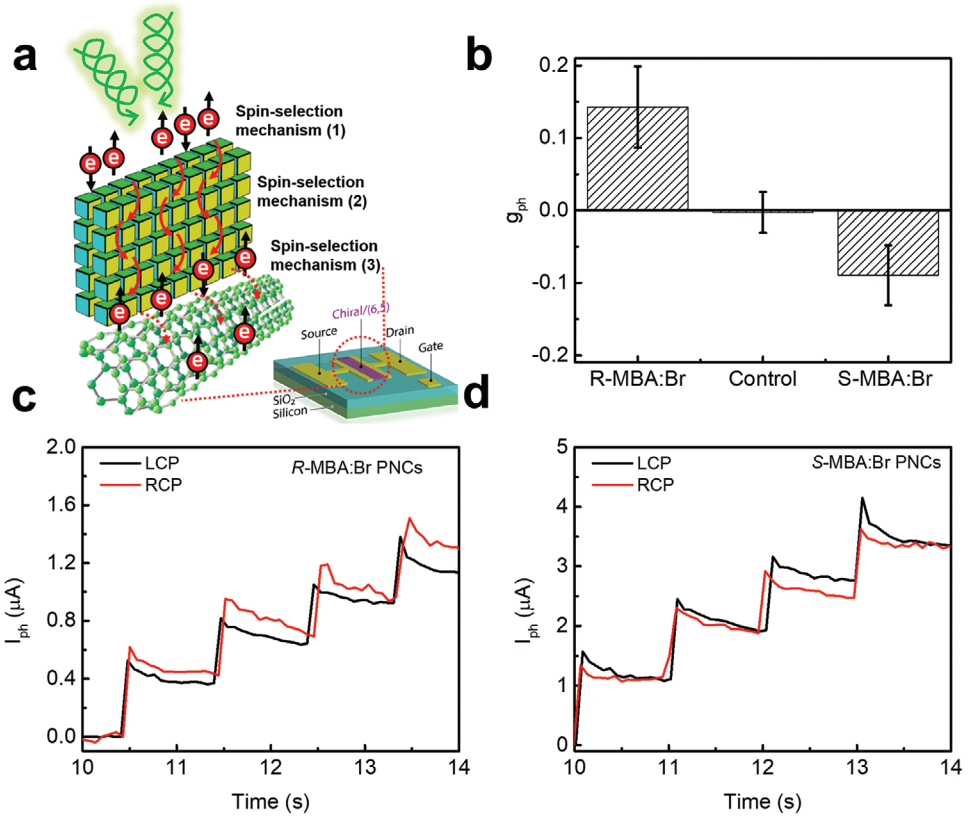

Figure 5. a) Schematics of structure of CPL detectors based on PNCs/semiconducting single-walled carbon nanotube (SWCNT) heterostructures and spin selection mechanisms in the devices. Here we excited the samples with CPL laser at 405 nm wavelength. b) Calculated g_{ph} in CPL detecting field-effect transistor (FET) devices based on R-/S-/control $CsPbBr_3$ PNC/SWCNT heterostructures. Time-dependent photocurrent changes of CPL detectors based on c) R-PNC/SWCNT heterojunctions and d) S-PNC/SWCNT heterojunctions. Here, measurements were done under 405 nm right-handed CPL and left-handed CPL pulse laser illumination with $V_{DS} = 1$ V.

heterojunctions is much higher than the optical anisotropy factor, g_{CD}, of R-PNC and S-PNC, which is normalized by considering CD response with respect to absorbance as below;

$$g_{CD} = 2 \times \frac{CD\,(mdeg)}{32\,980 \times absorbance\,(\text{o.d.})} \tag{4}$$

The g_{CD} of R-PNC and S-PNC at 405 nm which is used for exciting CPL detectors is $\pm 5 \times 10^{-5}$ (Figure S15, Supporting Information). In addition to spin-selection mechanism (1) (controlled absorption of CPL in R-/S-PNC films), we investigated other possible reasons of much higher g_{ph} of photo-transistors based on R-PNC/SWCNT heterojunctions and S-PNC/SWCNT heterojunctions than g_{CD} of R-PNC and S-PNC. It is possible that the spin polarization of charge carriers, which are selectively excited by right-handed CPL and left-handed CPL, is amplified when moving through multiple chiral PNCs in films (mechanism (2) in Figure 5a).[31,32] The mechanism of spin polarization of charge carriers when moving through the chiral materials/potentials/quantum dots is called chiral-induced spin-selectivity (CISS).[32–34] To investigate CISS in chiral PNC thin films, we fabricated devices based on the following structure [nickel (Ni) (≈50 nm)/aluminum oxide (1.5 nm)/ R-/S-/control-PNC films (≈50 nm which is around 5 layers of PNC (size ≈ 10 nm) thin films)/bathocuproine (≈50 nm)/molybdenum trioxide (≈15 nm)/Al (100 nm)] (Figures S16–S19, Supporting Information and associated discussion) and measured the current of the devices by changing the magnetization directions of the Ni electrode. From these measured currents, we calculate the degree of spin-polarized current, P_{spin}, as

$$P_{spin} = \frac{I_{up} - I_{down}}{I_{up} + I_{down}} \times 100\% \tag{5}$$

where I_{up} and I_{down} are the average current values of 10 measurements at 2 V when the Ni electrode was pre-magnetized in the up- or down-direction, respectively. P_{spin} is calculated to be 15.6% and –11.3% at 2 V for CISS devices based on R-PNC and S-PNC films, respectively. The higher P_{spin} in R-PNCs than that in S-PNCs is within the error of measurement, like the higher g_{ph} in R-PNCs/SWCNT heterojunctions (Figure 5b). Note that R-/S-MBA:Br do not form self-assembled thin films in the same way as assembled supramolecular polymer fibers[35,36] and double-stranded DNA monolayers.[37] Since these are small organic molecules with low charge conductivity, conductance in our films should occur through the PNCs. However, the mechanism of CISS is not fully understood and it is not yet known if the ligands could aid in CISS as charges propagate through them or if it is merely a structural/interfacial effect associated with the PNCs. Charge transfer between

chiral PNCs and SWCNT can be spin selective (mechanism (3) in Figure 5a).[33,38] Although one may expect that chirality in SWCNT[39] could contribute to the CISS current and CPL detectivity in photodetectors based on R-/S-PNC/SWCNT heterojunctions, we used the same racemic SWCNT samples for both R-PNC/SWCNT heterojunctions and S-PNC/SWCNT heterojunctions in photodetectors and furthermore measured chiral-induced spin-selectivity current in PNC films without SWCNTs. Therefore, we attribute the higher g_{ph} of phototransistors based on PNC/SWCNT heterojunctions than g_{CD} of PNCs to a combination of the three different mechanisms as explained above.

3. Conclusion

In conclusion, we couple theoretical simulations to the experimentally observed chiroptical response and photophysical properties of colloidal chiral $CsPbBr_3$ PNC thin films to formally understand the chiral transfer mechanism. R-/S-MBA:Br chiral ligands transfer chirality into PNCs by distorting the five outermost layers of surface octahedra, resulting in a symmetry breaking and slightly reduced bandgap. We find that chiral surface ligands increase the PLQE of PNCs by suppressing nonradiative recombination and facilitating radiative recombination. Additionally, we show that chiral PNCs can work as a CPL detector with detectivity of up to 14%. Our experimental and theoretical approach toward understanding the effects of chiral ligands on PNCs provides a path toward further spin-optoelectronics based on colloidal PNCs.

4. Experimental Section

Chemicals: Cesium carbonate (Cs_2CO_3; 99.9%), oleic acid (OA, technical grade 90%), oleylamine (OAm, technical grade 70%), 1-octadecene (ODE, technical grade 90%), hexane (reagent grade ≥95%), octane (anhydrous, ≥99%), methyl acetate (MeOAc, anhydrous 99.5%), ethyl acetate (EtOAc, anhydrous 99.5%), R-methybenzylamine (98% purity), S-methybenzylamine (98% purity), hydrobromic acid (ACS reagent, 48%), deuterated chloroform (99.8 at%), and ethyl acetate (EtOAc, anhydrous, 99.8%) were purchased from Sigma Aldrich. (R)-2-octylamine (98% purity) was purchased from Alfa Aesar.

Synthesis of Cs-Oleate Precursor: In a three-neck round-bottom flask, 1.25 mmol (0.407 g) of Cs_2CO_3, 1.25 mL of OA, and 20 mL of ODE were degassed under a vacuum at room temperature and 50 °C for 30 min, respectively. The temperature was then increased to 120 °C under N_2 and held at this temperature.

Synthesis of $CsPbBr_3$ PNCs: In a three-neck round-bottom flask, 1.08 mmol (0.398 g) $PbBr_2$ and 25 mL 1-ODE were degassed under vacuum at room temperature and 120 °C for 30 min, respectively. Mixtures of 2.5 mL of OA and 2.5 mL of OAm were preheated to 120 °C, then injected into the $PbBr_2$ mixture under vacuum. After $PbBr_2$ was fully dissolved, the solution became clear. Then the temperature of the solution was increased to 180 °C under N_2 flow. At 180 °C, 2 mL of the Cs-oleate stock solution was swiftly injected into the $PbBr_2$ mixture, which was then quenched by immersing the flask in an ice bath. After cooling to room temperature, 50 mL of methylacetate was added to the solution. The solution was centrifuged at 7500 rpm for 5 min to remove unreacted ligands and 1-ODE. The precipitate was dispersed in 5 mL of hexane, mixed with mL of methylacetate, and then centrifuged at 7500 rpm for 5 min again. The precipitate was dispersed in 5 mL of hexane and centrifuged at 7500 rpm for 5 min to remove the precipitated large particles. The 2nd purified supernatant solution with ≈10 nm of PNCs was collected and stored in a refrigerator.

Synthesis of R-/S-MBA:Br: In a single-neck round-bottom flask in an ice bath, 78 mmol (10 mL) R-,S-MBA and 30 mL of ethanol were added, then 116 mmol (13.2 mL) HBr aqueous solution was added dropwise into the flask under vigorous stirring. The solution was kept stirred in an ice bath overnight. The yellowish precipitate was collected by evaporation of solvents at 70 °C for 30 min, then washed thoroughly by repeating re-dissolution in ethanol and recrystallization in diethyl ether until colorless. The white precipitate was dissolved in a small amount of hot ethanol to make saturated solution, then recrystallized in a freezer; temperature drop reduced the saturation concentration of R-/S-MBA:Br in ethanol and induced recrystallization. The recrystallized precipitate was dried under vacuum overnight.

Solid-State Ligand-Treatment on $CsPbBr_3$ PNC films: To conduct the solid-state ligand-treatment on $CsPbBr_3$ PNC films, a saturated solution of R-/S-MBA:Br in EtOAc was prepared by sonicating 200 mg R-/S-MBA:Br in 20 mL of EtOAc, then centrifuging at 7500 rpm for 5 min. The supernatant solution was collected and spincoated on the 50-nm $CsPbBr_3$ PNC films.

^1H NMR Spectroscopy: For the sample preparation, 160 µL of a saturated R-/S-MBA:Br solution in EtOAc was mixed with 300 µL of purified $CsPbBr_3$ PNCs. The mixture was shaken mildly for 5 min at room temperature and then all solvent was evaporated under vacuum overnight. The dry precipitates were re-dispersed in 700 µL of deuterated chloroform and centrifuged to get rid of turbid particles direct before NMR measurement. NMR were taken on a Bruker 400 Avance III NMR using a standard proton pulse (zg), 64 scans, 4.0 s collection times, and a 25.0 s delay between scans at 25 °C. Deuterochloroform (d-CF, 99.8%, Sigma Aldrich) was used for the measurement.

Time-Resolved Photoluminescence: The samples were excited at 450 nm at a low frequency ($<<10^{15}$ s^{-1}) using a supercontinuum fiber laser (NKT Photonics, Super K) operating at 5 MHz as the excitation source. The emission was collected with a Hamamatsu C10910–04 streak camera. All samples were measured under same excitation conditions.

Photoluminescence Quantum Efficiency: PLQEs of $CsPbBr_3$ PNC films were measured using a 100-mm integrating sphere (Labsphere) integrated with the spectrometer (SpectraPro HRS 500, Princeton Instruments). $CsPbBr_3$ PNC films were excited using a 450-nm Xe-lamp.

Fourier-Transform Infrared Spectroscopy: FTIR measurements were done in an Ar glovebox on a Bruker Alpha FTIR spectrometer using a diffuse reflectance infrared Fourier transform spectrometer attachment with a resolution of 4 cm^{-1}. Background measurements were taken on blank Si substrates and subsequent sample measurements were taken as an average of 24 scans. Background measurements were taken of air and subsequent sample measurements were taken as an average of 24 scans.

Circular Dichroism Spectroscopy: CD measurements were carried out using a Jasco J-715 spectropolarimeter with the samples suspended as a film placed in the beam path. The CD spectra of different constructs were monitored from 300 to 650 nm with resolution of 0.2 nm and measurement speed of 100 nm s^{-1}.

Fabrication and Measurement of (6,5) Semiconducting SWCNTs/PNC Hybrid Films Based Photo-Transistors: Semiconducting SWCNT networks were pre-prepared by spraying the prepared s-SWCNT inks to the prepared substrate (SiO_2/Si wafer or quartz substrate) using the ultrasonic sprayer with a Sonotek 120 kHz impact nozzle by following the authors' previous literature.[29] On the deposited SWCNTs networks, the $CsPbBr_3$ PNCs which were dispersed in octane were spincoated to fabricate 50 nm thick-films and the saturated solution of R-/S-MBA:Br in EtOAc was spincoated on the 50-nm $CsPbBr_3$ PNC films. The 405 nm laser (KOKUYO laser diodes) was passed through a linear polarizer (Thorlabs Inc.) to generate linearly polarized light which was converted to CPL by passing through a 405 nm quarter wave plate (Thorlabs Inc.). The direction of CPL was changed by rotating the quarter wave plate prior to excitation to the SWCNTs/PNC heterostructure samples. The power of the left-handed and right-handed CPL was calibrated using a Field Mate laser power meter (Coherent Inc.).

First-Principles Calculations: The all-electron electronic structure code FHI-aims[40] was employed to perform the first-principles DFT calculations. All calculations were based on numeric atom-centered orbital (NAO) basis sets and intermediate default settings. The 15-layer $CsPbBr_3$ slab models in this study were constructed from the relaxed unit cell of the orthorhombic bulk $CsPbBr_3$ (see Table S4, Supporting Information).[41] The atomic structure was optimized based on DFT-PBE with a modified TS dispersion correction (TS-Cs, see below for details) and a $(3 \times 1 \times 3)$ *k*-point grid, where the grid dimension "1" corresponds to the stacking direction perpendicular to the slab and the other two dimensions correspond to the in-plane directions. For energy band structure calculations, the HSE06 hybrid density-functional[26] (with 25% Hartree-Fock exchange and a screening parameter of 0.11 $bohr^{-1}$) was employed as implemented in FHI-aims,[42] plus second-variational non-self-consistent SOC[27] and again, the $(3 \times 1 \times 3)$ *k*-point grid. This set of methods provides a good balance between computational cost and accuracy for hybrid organic–inorganic perovskite systems.

Modified Tkatchenko–Scheffler Dispersion Correction for Cs (TS-Cs): The TS vdW correction[24] is a widely used approach to capture dispersion interactions in density functional calculations, especially for the calculations including organic molecules. For systems not including alkali cations, the authors have found computationally optimized geometries in close agreement (1% or better) with experimentally determined counterparts.[25,43–46] This correction is defined as a sum over pairwise atomic interactions. Importantly, the vdW radius R^0_{free} of each element enters the TS formulation. However, as shown in Table S4, Supporting Information, the R^0_{free} value for Cs in the original TS scheme is very low. This difference leads to an unphysical overestimation of the binding energy between Cs atoms and ionic species derived from them (see Figures S7,S8, Supporting Information). Recently, the Tkatchenko group proposed an alternative way of determining R^0_{free} from atomic dipole polarizabilities.[47] As shown in Figures S7,S8, Supporting Information, this revised R^0_{free} yields much more realistic binding energy characteristics of Cs-containing dimers. Specifically, random phase approximation binding energy curves (RPA@PBE) were calculated,[48] that is, a level of man-body perturbation theory beyond DFT that naturally accounts for vdW dispersion interactions (Figure S7, Supporting Information). The RPA@PBE binding energies were then compared to binding energy curves calculated by DFT-PBE (no dispersion correction), by the original DFT-PBE + TS scheme, and by the DFT-PBE + TS scheme but with a revised R0free for Cs, here called "DFT-PBE + TS-Cs". FHI-aims' "tight" numerical defaults and NAO basis sets were used for the DFT comparison. Figure S8, Supporting Information shows that the revised PBE + TS-Cs vdW scheme performs much better for Cs-based dimers than the original PBE + TS scheme. As a further step, $CsPbBr_3$ bulk unit cells were also fully relaxed using the DFT-PBE + TS and DFT-PBE + TS-Cs approaches. The structure optimization used $4 \times 4 \times 4$ *k*-point grids and FHI-aims' "tight" numerical defaults. As shown in Table S4, Supporting Information, the DFT-PBE + TS-Cs unit cell agrees well with the experimental one.[41] The DFT-PBE + TS-Cs scheme was therefore used to represent both organic and organic–inorganic interactions in the simulations.

Supporting Information

Supporting Information is available from the Wiley Online Library or from the author.

Acknowledgements

Y.-H.K. and R.S. contributed equally to this work. This work was funded by the Center for Hybrid Organic Inorganic Semiconductors for Energy (CHOISE), an Energy Frontier Research Center funded by the Office of Basic Energy Sciences, Office of Science within the US Department of Energy. This work was authored in part by the National Renewable Energy Laboratory, operated by Alliance for Sustainable Energy, LLC, for the US Department of Energy (DOE) under Contract No. DE-AC36-08GO28308. In addition, the authors would like to thank the University of North Carolina at Chapel Hill and the Research Computing group for providing computational resources (the Dogwood cluster) and support that have contributed to these research results. Y.-H.K. also acknowledges the National Research Foundation of Korea (NRF) grant funded by the Korea government (MSIT) (2022R1C1C1008282) upon the commencement of his appointment at Hanyang University. The views expressed in the article do not necessarily represent the views of the DOE or the US Government.

Conflict of Interest

The authors declare no conflict of interest.

Data Availability Statement

The data that support the findings of this study are available from the corresponding authors upon reasonable request. Computational input and output data for DFT-based geometry relaxations and band structure calculations are available from the NOMAD repository (https://doi.org/10.17172/NOMAD/2022.02.20-2).

Keywords

chiral ligands, chiral transfer mechanism, circularly polarized light detector, colloidal perovskite nanocrystals, lattice distortion

Received: January 13, 2022
Revised: March 1, 2022
Published online: March 16, 2022

[1] Y. Zhai, S. Baniya, C. Zhang, J. Li, P. Haney, C.-X. Sheng, E. Ehrenfreund, Z. V. Vardeny, *Sci. Adv.* **2017**, *3*, e1700704.
[2] D. Niesner, M. Wilhelm, I. Levchuk, A. Osvet, S. Shrestha, M. Batentschuk, C. Brabec, T. Fauster, *Phys. Rev. Lett.* **2016**, *117*, 126401.
[3] P. Odenthal, W. Talmadge, N. Gundlach, R. Wang, C. Zhang, D. Sun, Z.-G. Yu, Z. Valy Vardeny, Y. S. Li, *Nat. Phys.* **2017**, *13*, 894.
[4] M. Isarov, L. Z. Tan, M. I. Bodnarchuk, M. V. Kovalenko, A. M. Rappe, E. Lifshitz, *Nano Lett.* **2017**, *17*, 5020.
[5] A. Swarnkar, A. R. Marshall, E. M. Sanehira, B. D. Chernomordik, D. T. Moore, J. A. Christians, T. Chakrabarti, J. M. Luther, *Science* **2016**, *354*, 92.
[6] Y.-H. Kim, S. Kim, A. Kakekhani, J. Park, J. Park, Y.-H. Lee, H. Xu, S. Nagane, R. B. Wexler, D.-H. Kim, S. H. Jo, L. Martínez-Sarti, P. Tan, A. Sadhanala, G.-S. Park, Y.-W. Kim, B. Hu, H. J. Bolink, S. Yoo, R. H. Friend, A. M. Rappe, T.-W. Lee, *Nat. Photon.* **2021**, *15*, 148.
[7] Y.-H. Kim, Y. Zhai, E. A. Gaulding, S. N. Habisreutinger, T. Moot, B. A. Rosales, H. Lu, A. Hazarika, R. Brunecky, L. M. Wheeler, J. J. Berry, M. C. Beard, J. M. Luther, *ACS Nano* **2020**, *14*, 8816.
[8] W. Chen, S. Zhang, M. Zhou, T. Zhao, X. Qin, X. Liu, M. Liu, P. Duan, *J. Phys. Chem. Lett.* **2019**, *10*, 3290.
[9] Y. Shi, P. Duan, S. Huo, Y. Li, M. Liu, *Adv. Mater.* **2018**, *30*, 1705011.
[10] P. Liu, W. Chen, Y. Okazaki, Y. Battie, L. Brocard, M. Decossas, E. Pouget, P. Müller-Buschbaum, B. Kauffmann, S. Pathan, T. Sagawa, R. Oda, *Nano Lett.* **2020**, *20*, 8453.

[11] Z. N. Georgieva, B. P. Bloom, S. Ghosh, D. H. Waldeck, *Adv. Mater.* **2018**, *30*, 1800097.
[12] R. Prasanna, A. Gold-Parker, T. Leijtens, B. Conings, A. Babayigit, H. G. Boyen, M. F. Toney, M. D. McGehee, *J. Am. Chem. Soc.* **2017**, *139*, 11117.
[13] R. Grisorio, M. E. Di Clemente, E. Fanizza, I. Allegretta, D. Altamura, M. Striccoli, R. Terzano, C. Giannini, M. Irimia-Vladu, G. P. Suranna, *Nanoscale* **2019**, *11*, 986.
[14] J. De Roo, M. Ibáñez, P. Geiregat, G. Nedelcu, W. Walravens, J. Maes, J. C. Martins, I. Van Driessche, M. V. Kovalenko, Z. Hens, *ACS Nano* **2016**, *10*, 2071.
[15] S. R. Smock, T. J. Williams, R. L. Brutchey, *Angew. Chem., Int. Ed.* **2018**, *57*, 11711.
[16] J. Coates, *Encyclopedia of Analytical Chemistry*, Wiley, Hoboken **2006**.
[17] V. S. Chirvony, S. González-Carrero, I. Suárez, R. E. Galian, M. Sessolo, H. J. Bolink, J. P. Martínez-Pastor, J. Pérez-Prieto, *J. Phys. Chem. C* **2017**, *121*, 13381.
[18] D. Sahoo, K. Sugiyasu, Y. Tian, M. Takeuchi, I. G. Scheblykin, *Chem. Mater.* **2014**, *26*, 4867.
[19] J. Ma, C. Fang, C. Chen, L. Jin, J. Wang, S. Wang, J. Tang, D. Li, *ACS Nano* **2019**, *13*, 3659.
[20] A. Ben Moshe, G. Markovich, *Isr. J. Chem.* **2012**, *52*, 1104.
[21] B. A. Koscher, J. K. Swabeck, N. D. Bronstein, A. P. Alivisatos, *J. Am. Chem. Soc.* **2017**, *139*, 6566.
[22] Y.-H. Kim, C. Wolf, Y.-T. Kim, H. Cho, W. Kwon, S. Do, A. Sadhanala, C. G. Park, S.-W. Rhee, S. H. Im, R. H. Friend, T.-W. Lee, *ACS Nano* **2017**, *11*, 6586.
[23] J. P. Perdew, K. Burke, M. Ernzerhof, *Phys. Rev. Lett.* **1996**, *77*, 3865.
[24] A. Tkatchenko, M. Scheffler, *Phys. Rev. Lett.* **2009**, *102*, 066402.
[25] M. K. Jana, R. Song, H. Liu, D. R. Khanal, S. M. Janke, R. Zhao, C. Liu, Z. Valy Vardeny, V. Blum, D. B. Mitzi, *Nat. Commun.* **2020**, *11*, 4699.
[26] J. Heyd, G. E. Scuseria, M. Ernzerhof, *J. Chem. Phys.* **2003**, *118*, 8207.
[27] W. P. Huhn, V. Blum, *Phys. Rev. Mater.* **2017**, *1*, 033803.
[28] D. M. Kroupa, M. Vörös, N. P. Brawand, N. Bronstein, B. W. McNichols, C. V. Castaneda, A. J. Nozik, A. Sellinger, G. Galli, M. C. Beard, *J. Phys. Chem. Lett.* **2018**, *9*, 3425.
[29] J. Hao, Y.-H. Kim, S. N. Habisreutinger, S. P. Harvey, E. M. Miller, S. M. Foradori, M. S. Arnold, Z. Song, Y. Yan, J. M. Luther, J. L. Blackburn, *Sci. Adv.* **2021**, *7*, eabf1959.
[30] E. A. Gaulding, J. Hao, H. S. Kang, E. M. Miller, S. N. Habisreutinger, Q. Zhao, A. Hazarika, P. C. Sercel, J. M. Luther, J. L. Blackburn, *Adv. Mater.* **2019**, *31*, 1902250.
[31] J. Hao, H. Lu, L. Mao, X. Chen, M. C. Beard, J. L. Blackburn, *ACS Nano* **2021**, *15*, 7608.
[32] H. Lu, J. Wang, C. Xiao, X. Pan, X. Chen, R. Brunecky, J. J. Berry, K. Zhu, M. C. Beard, Z. V. Vardeny, *Sci. Adv.* **2019**, *5*, eaay0571.
[33] R. Naaman, Y. Paltiel, D. H. Waldeck, *Nat. Rev. Chem.* **2019**, *3*, 250.
[34] B. P. Bloom, V. Kiran, V. Varade, R. Naaman, D. H. Waldeck, *Nano Lett.* **2016**, *16*, 4583.
[35] C. Kulkarni, A. K. Mondal, T. K. Das, G. Grinbom, F. Tassinari, M. F. J. Mabesoone, E. W. Meijer, R. Naaman, *Adv. Mater.* **2020**, *32*, 1904965.
[36] A. K. Mondal, M. D. Preuss, M. L. Ślęczkowski, T. K. Das, G. Vantomme, E. W. Meijer, R. Naaman, *J. Am. Chem. Soc.* **2021**, *143*, 7189.
[37] B. Göhler, V. Hamelbeck, T. Z. Markus, M. Kettner, G. F. Hanne, Z. Vager, R. Naaman, H. Zacharias, *Science* **2011**, *331*, 894.
[38] J. M. Abendroth, D. M. Stemer, B. P. Bloom, P. Roy, R. Naaman, D. H. Waldeck, P. S. Weiss, P. C. Mondal, *ACS Nano* **2019**, *13*, 4928.
[39] F. Yao, W. Yu, C. Liu, Y. Su, Y. You, H. Ma, R. Qiao, C. Wu, C. Ma, P. Gao, F. Xiao, J. Zhao, X. Bai, Z. Sun, S. Maruyama, F. Wang, J. Zhang, K. Liu, *Nat. Nanotechnol.* **2021**, *16*, 1073.
[40] V. Blum, R. Gehrke, F. Hanke, P. Havu, V. Havu, X. Ren, K. Reuter, M. Scheffler, *Comput. Phys. Commun.* **2009**, *180*, 2175.
[41] C. C. Stoumpos, C. D. Malliakas, J. A. Peters, Z. Liu, M. Sebastian, J. Im, T. C. Chasapis, A. C. Wibowo, D. Y. Chung, A. J. Freeman, B. W. Wessels, M. G. Kanatzidis, *Cryst. Growth Des.* **2013**, *13*, 2722.
[42] S. V. Levchenko, X. Ren, J. Wieferink, R. Johanni, P. Rinke, V. Blum, M. Scheffler, *Comput. Phys. Commun.* **2015**, *192*, 60.
[43] C. Liu, W. Huhn, K.-Z. Du, A. Vazquez-Mayagoitia, D. Dirkes, W. You, Y. Kanai, D. B. Mitzi, V. Blum, *Phys. Rev. Lett.* **2018**, *121*, 146401.
[44] M. K. Jana, S. M. Janke, D. J. Dirkes, S. Dovletgeldi, C. Liu, X. Qin, K. Gundogdu, W. You, V. Blum, D. B. Mitzi, *J. Am. Chem. Soc.* **2019**, *141*, 7955.
[45] M. K. Jana, C. Liu, S. Lidin, D. J. Dirkes, W. You, V. Blum, D. B. Mitzi, *Chem. Mater.* **2019**, *31*, 8523.
[46] M. K. Jana, R. Song, Y. Xie, R. Zhao, P. C. Sercel, V. Blum, D. B. Mitzi, *Nat. Commun.* **2021**, *12*, 4982.
[47] D. V. Fedorov, M. Sadhukhan, M. Stöhr, A. Tkatchenko, *Phys. Rev. Lett.* **2018**, *121*, 183401.
[48] X. Ren, P. Rinke, V. Blum, J. Wieferink, A. Tkatchenko, A. Sanfilippo, K. Reuter, M. Scheffler, *New J. Phys.* **2012**, *14*, 053020.